HEALTH AND MEDICINE

A combinational chemo-immune therapy using an enzyme-sensitive nanoplatform for dual-drug delivery to specific sites by cascade targeting

Yanmei He[1]*, Lei Lei[1,2]*, Jun Cao[1,3†], Xiaotong Yang[2], Shengsheng Cai[1], Fan Tong[2], Dennis Huang[3], Heng Mei[1], Kui Luo[4], Huile Gao[2†], Bin He[1], Nicholas A. Peppas[3,5†]

Nanoparticle-based drug delivery faces challenges from the imprecise targeted delivery and the low bioavailability of drugs due to complex biological barriers. Here, we designed cascade-targeting, dual drug–loaded, core-shell nanoparticles (DLTPT) consisting of CD44-targeting hyaluronic acid shells decorated with doxorubicin (HA-DOX) and mitochondria-targeting triphenylphosphonium derivative nanoparticle cores loaded with lonidamine (LND) dimers (LTPT). DLTPT displayed prolonged blood circulation time and efficiently accumulated at the tumor site due to the tumor-homing effect and negatively charged hyaluronic acid. Subsequently, the HA-DOX shell was degraded by extracellular hyaluronidase, resulting in decreased particle size and negative-to-positive charge reversal, which would increase tumor penetration and internalization. The degradation of HA-DOX further accelerated the release of DOX and exposed the positively charged LTPT core for rapid endosomal escape and mitochondria-targeted delivery of LND. Notably, when DLTPT was used in combination with anti–PD-L1, the tumor growth was inhibited, which induced immune response against tumor metastasis.

INTRODUCTION

In recent years, various nanoparticle-based drug delivery systems have been developed and widely used in cancer chemotherapy (*1*–*4*). Although nanoscale drug delivery systems can improve the bioavailability and tolerance of drugs, the efficacy of drug delivery is still restricted by the "CAPIR cascade," e.g., blood circulation, tumor accumulation, tumor penetration, tumor internalization of nanoparticles, and intracellular specific drug release (*5*–*7*). To overcome the obstacles associating with the CAPIR cascade, we developed cascade-targeting, dual drug–loaded, core-shell intelligent nanoparticles (DLTPT) with tumor-active targeting, enzyme-sensitive size modifications, charge reversal, and organelle-specific controlled-release properties. Hyaluronic acid (HA) was selected as the surface layer of DLTPT to facilitate the targeting of particles to CD44 receptor and the degradation by hyaluronidase (HAase), which are both overexpressed in the tumors (*8*, *9*). After degradation, the inner positively charged triphenylphosphonium derivatives particles (LTPT) with smaller size and negative-to-positive charge reversal were released to penetrate deep into the tumor, efficiently uptaken by tumor cells, followed by rapid endosomal escape. TPT was constructed by the self-assembly of the amphiphilic TPT polymer containing relatively hydrophilic triphenylphosphine (TPP) and biodegradable hydrophobic poly(L-lactic acid) (PLLA), in which the TPP could target the mitochondria for organelle-specific drug delivery and the PLLA could form hydrophobic cores to load drugs (*10*, *11*).

The combination of various intracellular-functioning small-molecule drugs has recently evolved as a burgeoning therapeutic strategy because it could lead to the destruction of specific subcellular structures via activating apoptotic signals (*12*, *13*). For instance, lonidamine (LND) interferes with mitochondrial function to activate apoptotic signaling by releasing cytochrome C into the cytoplasm and activating caspase-9, leading to the up-regulation of downstream caspase-3 (*14*, *15*). Similarly, doxorubicin (DOX) induces apoptosis via nuclear oxidative DNA damage, which could cause indirect hydrogen peroxide (H_2O_2) generation through poly ADP (adenosine diphosphate)–ribose polymerase (PARP) and triphosphopyridine nucleotide (NADPH) oxidase activation, leading to an increase in mitochondrial membrane potential and subsequent caspase-3 activation (*16*). Therefore, DOX and LND might show a synergistic antitumor effect. However, small-molecule drugs show no organ selectivity, thus typically failing to accumulate in specific organelles (*17*). To specifically deliver DOX and LND into different organelles, DOX was conjugated onto the HA chains to form the shell of DLTPT, which would release DOX into the cytoplasm, followed by its targeting to the nucleus, and LND was encapsulated within the TPT core via π-π stacking and electrostatic interactions, which would specifically deliver LND to the mitochondria. However, the weak interaction between small-molecule drugs and amphiphilic copolymers results in the low drug loading capacity (DLC) of LND (*18*, *19*). Therefore, LND dimer (d-LND) was synthesized using the sulfur bond as the linker to improve the DLC, and d-LND could intelligently produce LND in response to intracellular glutathione (GSH) to achieve specific release (*20*–*22*).

Chemotherapeutic agents, such as anthracyclines, are known to induce immunogenic cell death (ICD) (*23*–*25*). ICD can induce an immune response through the activation of dendritic cells (DCs) and the consequent activation of a T cell–specific response (*26*–*28*). However, the antitumor effect of tumor-reactive cytotoxic T cells was limited because of the overexpression of programmed cell death 1 ligand 1 (PD-L1) on cancer cells, which interacts with programmed cell death receptor 1 (PD-1) on T cells and induces T cell apoptosis (*29*–*31*). PD-L1 antibodies (anti–PD-L1) can block the immune

[1]National Engineering Research Center for Biomaterials, Sichuan University, Chengdu 610064, P. R. China. [2]West China School of Pharmacy, Sichuan University, Chengdu 610041, P. R. China. [3]Department of Biomedical Engineering, The University of Texas at Austin, Austin, TX 78731, USA. [4]Huaxi MR Research Center (HMRRC), Functional and Molecular Imaging Key Laboratory of Sichuan Province, Department of Radiology, West China Hospital, Sichuan University, Chengdu 610041, P. R. China. [5]Division of Molecular Pharmaceutics and Drug Delivery, College of Pharmacy, The University of Texas at Austin, Austin, TX 78731, USA.
*These authors equally contributed to this work.
†Corresponding author. Email: caojun@scu.edu.cn (J.C.); gaohuile@scu.edu.cn (H.G.); peppas@che.utexas.edu (N.A.P.)

evasion of cancer cells by inhibiting the activities of immune-suppressive regulatory T cells (T_{regs}) and reactivating cytotoxic T lymphocytes (CTLs) (*32*, *33*). However, the low therapeutic response (~20%) of using only anti–PD-L1 limits its clinical applications (*34*–*35*). Studies have reported that a combination of chemotherapy and immunotherapy could effectively activate more CTLs, resulting in a better antitumor effect (*36*, *37*).

In this study, we designed a system of cascade-targeting, dual drug–loaded, core-shell intelligent nanoparticles (DLTPT) to precisely deliver multiple drugs to tumor-specific sites (Fig. 1). After intravenous injection, the HA surface of DLTPT enabled a long blood circulation time and a high tumor accumulation owing to the negative surface charge and CD44-specific tumor-targeting properties. Within the tumor, the degradation of HA-DOX by HAase benefited the particle size decrease in DLTPT and negative-to-neutral charge reversal, leading to improved tumor penetration and cellular internalization. After tumor cells uptook DLTPT, HAase continuously degraded HA-DOX to release DOX near nuclei, while TPT carried d-LND into the mitochondria for the redox-responsive release of LND. Therefore, DOX and LND release at their specific action sites can synergistically induce cell apoptosis and ultimately inhibit tumor growth. Besides, DOX can also activate an immune response; moreover, the addition of anti–PD-L1 can further block PD-L1–dependent immune evasion and improve the immune response by activating CTLs. In vivo studies have shown that dual-drug chemotherapy, combined with immunotherapy, improved the efficiency of tumor inhibition and induced antitumor immune response against tumor metastasis.

RESULTS

Molecular engineering and multifunctional features of DLTPT

DLTPT was constructed as shown in Fig. 1A. Briefly, the d-LND and TPT polymer self-assembled in water to form LTPT core first, which was then decorated with HA-DOX shell layer via electro-interaction of HA-DOX and LTPT. The specific synthetic routes of the functional molecules (TPT polymer, d-LND, and HA-DOX) are illustrated in fig. S1. The proton nuclear magnetic resonance (^{1}H NMR) spectrum of the TPT polymer showed crucial PLLA peaks at about δ = 5.2 parts per million (ppm), 1.5 ppm, and $(C_6H_5)_3$-P^+- in the TPP moiety at δ = 7.7 to 7.9 ppm (fig. S2A), demonstrating the successful synthesis of this product. The ^{1}H NMR spectrum of d-LND showed distinguishing peaks at about δ = 3.0 ppm and δ = 5.9 ppm, which corresponded to the methylene near the amide and benzene ring, respectively (fig. S2B). The mass spectrum result was consistent with the calculated molecular weight of d-LND, indicating that this substance was successfully synthesized (fig. S2C). The ^{1}H NMR and ultraviolet (UV) spectra of HA-DOX demonstrated the successful bonding of DOX with HA (fig. S2D).

TPT, with a size of 92 nm and zeta potential of 55 mV at a micellar concentration of 0.75 mg ml^{-1}, was selected to further construct the suitable nanosized hierarchical nanocomposite (fig. S3A). The DLC of LND in TPT (ITPT) was less than 2%, but the DLC of d-LND in TPT (LTPT) was 4.5 times higher than that of LND, demonstrating that the dimer drug could greatly enhance the drug loading ability (fig. S3B). Moreover, the aggregation-caused quenching phenomena of d-LND fluorescence in LTPT indicated the formation of compact LTPT with π-π stacking in water (fig. S3C). In addition, the decreased zeta potential and the increased particle size (Fig. 2, A and B) demonstrated the successful formation of LTPT, which was also verified by transmission electron microscopy (TEM) (Fig. 2, D-1). Meanwhile, when the mass ratio of d-LND and TPT polymer was 1:5, LTPT showed the highest DLC and prominent physicochemical properties (fig. S4, A and B).

Subsequently, negatively charged HA-DOX was coated on the surface of LTPT to construct DLTPT. The cytotoxicity was examined in various combination ratios of DOX and d-LND, and the best synergy index was 0.652 when the mass ratio of DOX and d-LND

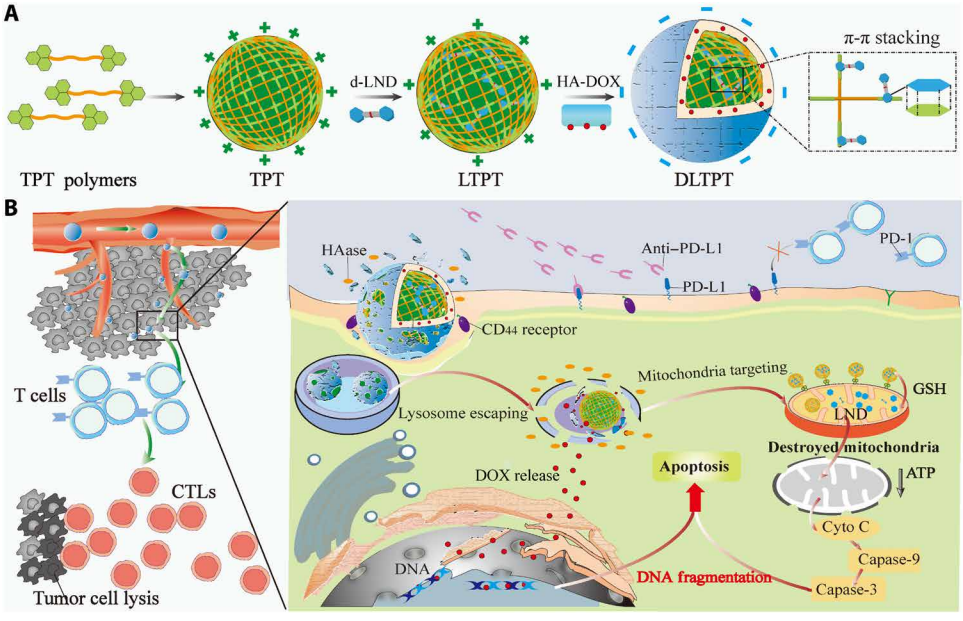

Fig. 1. Schematic diagram of dual-drug chemo- and immune-combinational therapy mechanism. (**A**) Schematic illustration for the self-assembly process of the cascade-targeting enzyme-sensitive hierarchical nanoplatform. (**B**) Schematic illustration of the combinational effects including chemotherapeutics in combination with anti–PD-L1 for activating the immune system to maximize the chemo-immune therapeutics. Cyto C, cytochrome C.

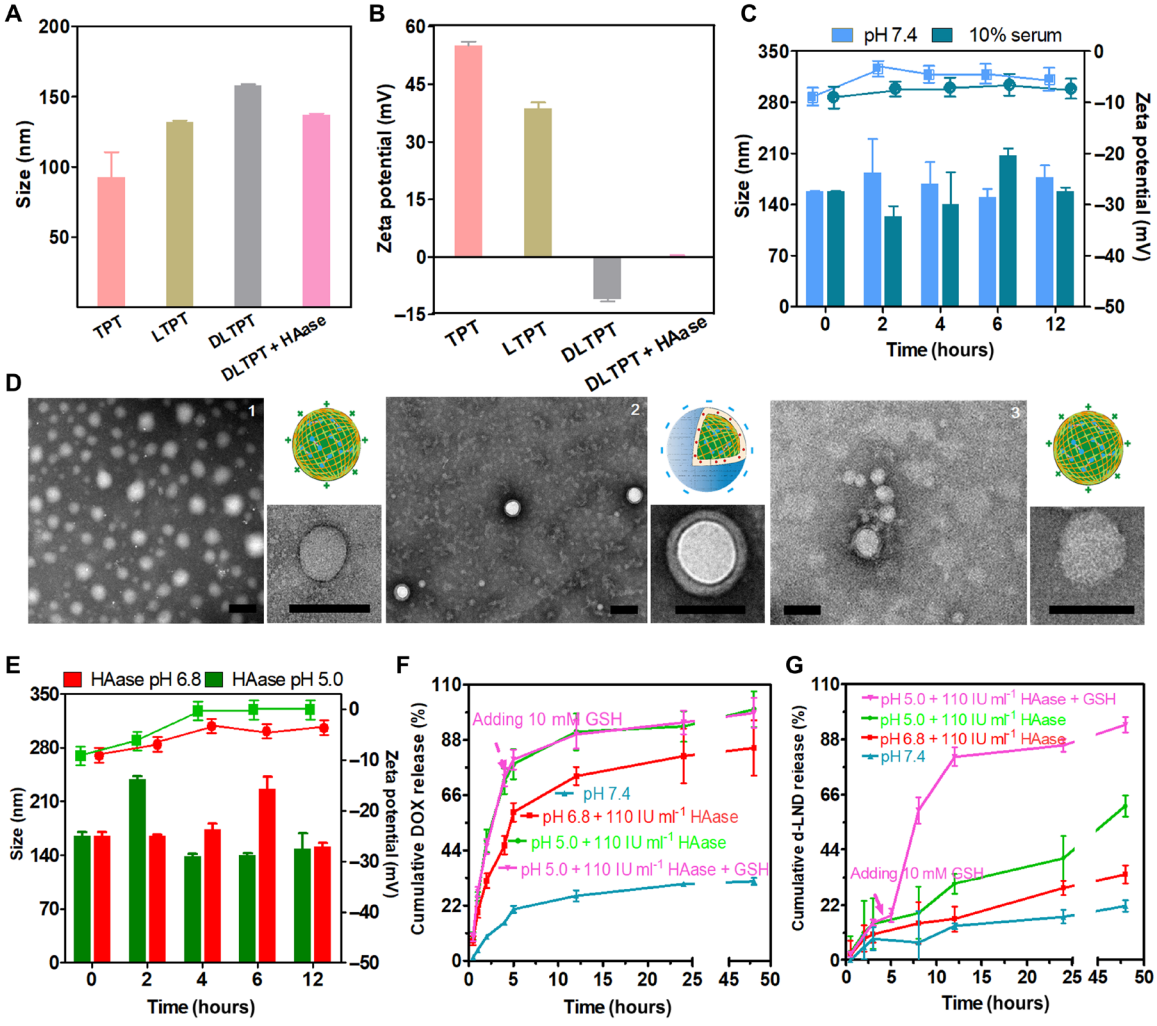

Fig. 2. Characterization the multifunctional properties of nanoparticles. (**A**) Particle sizes and (**B**) zeta potential of TPT, LTPT, DLTPT, and HAase + DLTPT. (**C**) Stability of DLTPT in pH 7.4 PBS and 10% serum-rich media. (**D**) Transmission electron microscopy (TEM) images and sizes of LTPT (1), DLTPT (2), and DLTPT preincubated with HAase at pH 5.0 buffer solution (3). Scale bars, 200 nm (left) and 100 nm (right). (**E**) Particle sizes and zeta potentials of DLTPT within HAase buffer solution (pH 5.0 and pH 6.8). (**F**) DOX release and (**G**) d-LND release profiles of DLTPT under different conditions.

was 2:1 (fig. S4C). Thereby, a mass ratio of 2:1 was selected for the construction of DLTPT. The zeta potential of DLTPT decreased from 39 to −12 mV, and the size increased to ~160 nm after coating HA-DOX (Fig. 2, A and B). The TEM results showed an obvious core-shell spherical nanostructure for DLTPT (Fig. 2, D-2), indicating the formation of a compact hierarchical nanocomposite via electrostatic interactions.

Compared with LTPT, DLTPT maintained good dimensional stability and a negative zeta potential in the neutral, serum-rich medium and diluted solution (Fig. 2C and fig. S5), implying that DLTPT would be able to prolong the blood circulation time. In addition, the incubation of DLTPT with HAase (110 IU ml^{-1}) resulted in the decrease in the diameter and increase in the zeta potential (~0 mV) (Fig. 2, A and B), which can be attributed to the HAase-triggered degradation of the HA corona. Moreover, the morphology of DLTPT after HAase incubation visualized using TEM confirmed the degradation behavior as well (Fig. 2, D-3). Both the particle size and the zeta potential of DLTPT varied faster at pH 5.0 than that at pH 6.8 (Fig. 2E), indicating that acidic conditions accelerated HAase-catalyzed HA degradation. The increased zeta potential and the decreased particle size may promote tumor penetration and lysosome escape, thus enhancing mitochondria-targeted delivery of drugs.

In vitro DOX and d-LND release profiles were evaluated in various biomimetic buffer solutions (Fig. 2, F and G). The DOX and d-LND release percentages of DLTPT were about 25 and 15% in a buffer of pH 7.4, respectively, indicating that DLTPT retain a majority of the loaded drugs in neutral medium. On the contrary, both HAase and acidic media induced fast release of DOX (almost 100%) and d-LND (~50%) over 48 hours because of the degradation of the HA corona and the protonation of DOX. Slower LND released from DLTPT in HAase and acidic environments guaranteed that LND could be efficiently delivered to mitochondria by LTPT. The release percentage of the accumulated LND released from DLTPT was almost 90% when GSH was added into the media, stating that the loaded LND in LTPT would be efficiently released in mitochondria. Collectively, DLTPT can prevent premature leakage of antitumor drugs and deliver drugs into tumor and subcellular sites.

In vitro antitumor efficiency of DLTPT measured by the 3-(4,5-dimethyl-2-thiazolyl)-2,5-diphenyl-2-*H*-tetrazolium bromide (MTT) assay is shown in fig. S6A. The half-maximal inhibitory concentration (IC_{50}) of DLTPT was 2.6 μg ml^{-1}, which was lower than that of DTPT (5.1 μg ml^{-1}), contributed by the combinational effect of DOX and LND. However, after preincubating 4T1 cells with HA, the IC_{50} of HA + DLTPT (5.8 μg ml^{-1}) nearly doubled, demonstrating that DLTPT could be efficiently internalized into cells via the CD44-mediated endocytic pathway. After observing that a combination of d-LND and DOX exhibited improved anticancer effects, we examined whether different formulations could induce 4T1 cell apoptosis using the annexin V–fluorescein isothiocyanate (FITC)/propidium iodide detection assay (fig. S6. B and C). Although the late apoptosis was nearly unchanged, the early apoptosis of DLTPT was 1.77-fold higher than DTPT, and overall apoptosis and necrosis were significantly higher than DTPT (**$P < 0.01$), which further demonstrated that the combinational effect between DOX and d-LND prompted cell apoptosis.

Cascade-targeting evaluation

Considering the satisfactory antitumor activity in 4T1 cells, we started to examine the mechanism behind our design to defeat cancer cells. As shown in the flow cytometry results (fig. S6D), the fluorescence intensities in 4T1 cells were increased with increased incubation time due to the optimal cellular internalization of DLTPT, indicating that cell membranes would be broken down by HA-activated DLTPT. Moreover, after incubating with 4T1 cells for 1 and 2 hours, the DOX fluorescence intensity of the DLTPT group was significantly higher than that of the HA + DLTPT groups (***$P < 0.001$ and *$P < 0.05$), further demonstrating that DLTPT could be internalized into cells via the CD44 receptor–mediated endocytosis pathway. The corresponding phenomena were further verified by qualitative evaluation of images obtained by confocal laser scanning microscopy (CLSM) (fig. S6E).

To verify the intracellular fate of DLTPT after internalization into cells, endo-lysosomal escape was recorded with a lysosomal staining kit by CLSM (Fig. 3A). After incubating for 2 hours, CLSM results showed that the majority of the green signal from DLTPT overlapped with the red signal from the lyso-tracker, indicating that surface HA promoted DLTPT cell internalization. However, after an additional 2-hour incubation (without nanoparticles), the overlap between the red and green signals was reduced, which was indicative of accelerated escape from the endo-lysosomal compartments. Moreover, the overlap between the red and green signals continued to decrease with increasing incubation time up to 4 hours.

The mitochondria-targeting capability of DLTPT was further examined by CLSM. Coumarin-3 (cou)–labeled DLTPT was formed by replacing d-LND with cou. After incubating 4T1 cells with cou-DLTPT for 2 hours, results showed slight overlapping fluorescence signal regions, while the fluorescence intensity of the overlapping regions increased with increasing incubation time (without nanoparticles) from 0 to 4 hours, indicating colocalization of red fluorescence for mitochondria and blue fluorescence for DLTPT (Fig. 3B). The increased overlapping fluorescence suggested that TPT could deliver the drug by targeting the mitochondria via an active-mediated pathway.

Thereafter, we examined the effects of DLTPT on mitochondrial function (Fig. 3, C to E, and fig. S6, F and G). First, the mitochondria membrane potentials (ΔΨm) were visualized by CLSM depending on the intracellular fluorescence intensity of JC-1. In comparison to the control group, much less red fluorescence was observed in the DLTPT and DTPT groups with higher red fluorescence being detected in the DTPT group compared with DLTPT (Fig. 3C). The reduction in fluorescence intensity in 4T1 cells with DLTPT treatment represented the depletion of mitochondrial transmembrane potential. Moreover, the combination of DOX and LND would provoke obvious disturbance on the mitochondrial membrane potentials of 4T1 cells. Subsequently, the decrease in ΔΨm in the DLTPT group facilitate the termination of adenosine triphosphate (ATP) production in 4T1 cells, thus restraining biological functions associated with ATP-driven cell growth (Fig. 3D). Furthermore, cytochrome C is a well-established apoptotic marker (*38*), which would be released into the cytoplasm to activate the downstream apoptotic signals. According to immunohistochemistry results, the level of cytochrome C in the DLTPT group is higher compared with that in other groups (Fig. 3E). Next, we also examined the protein levels of both caspase-3 and caspase-9, two important mediators of apoptosis. After treating with DLTPT, the caspase-3 and caspase-9 levels in 4T1 cells increased compared with the control groups (fig. S6, F and G). Collectively, the active-targeting delivery of LND to the mitochondria combination with DOX yielded combinational effects to effectively induce cell apoptosis.

In vitro immune response, penetration, and in vivo distribution evaluation

Motivated by previous reports that DOX can not only induce cancer cells death but also stimulate antitumor immunity by inducing ICD (*39*), the ability of inducing ICD was evaluated by immunofluorescence analysis. This analysis detects released endoplasmic reticulum chaperone calreticulin (CRT), a kind of damage-associated molecular patterns (DAMPs). Obvious release of CRT from their cytosol could be observed in 4T1 cells when incubated with DTPT and DLTPT (Fig. 4A), indicating the presence of effective ICD in cancer cells induced by our DOX formulations. Notably, increased exposure of CRT was observed after DLTPT treatment compared with DTPT treatment (*$P < 0.05$; fig. S7A), reflecting that the combination of DOX and LND could induce a higher level of ICD, which may activate DCs and tumor antigen presentation to subsequently boost antitumor immune response.

To further investigate the penetrating ability of our formulations, we evaluated nanoformulation penetration using multicellular tumor spheroids (MTSs) (Fig. 4, B to D). Strong fluorescence signals were detected in MTS within 4T1 cells exposed to DLTPT for 6 hours at a distance less than 40 μm, whereas weak fluorescence signals were observed from 40 to 70 μm because of the poor penetration of negatively charged DLTPT. After preincubating 4T1 cells with HAase (110 IU ml^{-1}) for 4 hours, a stronger fluorescence signal could be observed in the HAase + DLTPT group, even at 70 μm, indicating that the degradation of the HA corona by HAase enhanced nanoformulation penetration because of decreased size and increased zeta potential of DLTPT as demonstrated by dynamic light scattering (DLS) results (Fig. 2, A and B).

We then carefully explored the in vivo distribution of DLTPT. The distribution of fluorescence emitted from DOX in major organs at 24 and 36 hours after injection was tracked by using the in vivo fluorescence imaging system (Fig. 4, E and F, and fig. S7B). The fluorescence intensity of DLTPT within the tumor at 36 hours was 1.4-fold higher than that of TPP/DOX, indicating that HA

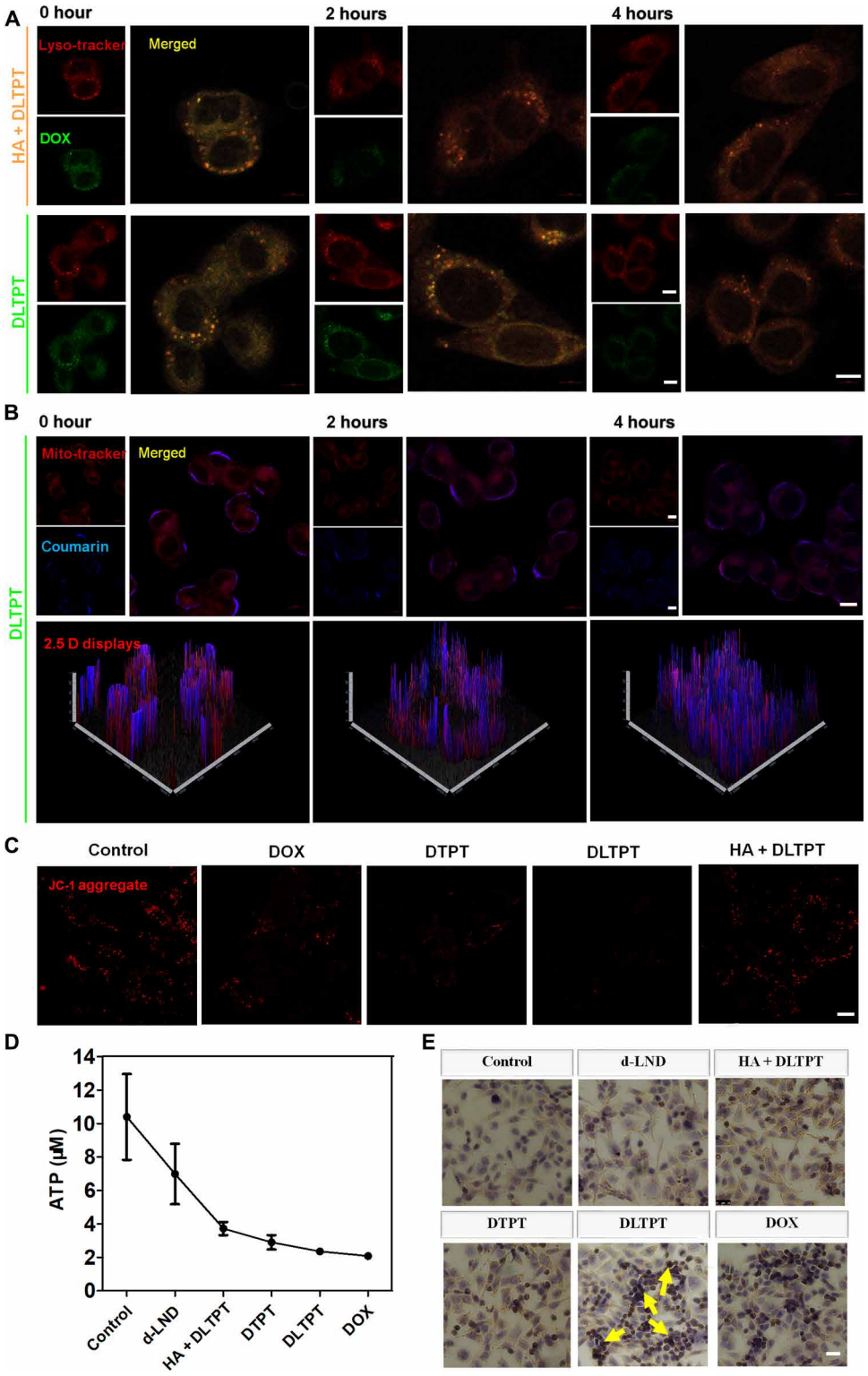

Fig. 3. Cascade-targeting and apoptosis mechanism evaluations of DLTPT in vitro. (**A**) The CLSM images of DLTPT and HA + DLTPT cultured with cells for 2 hours and then incubated with fresh medium without nanoparticles for an additional 0, 2, and 4 hours, where the lysosomal staining channel is red and the DOX channel is green. Scale bars, 5 μm. (**B**) CLSM images and 2.5 D displays of 4T1 cells after treatment with coumarin-3 (cou)–labeled DLTPT for 2 hours and then incubated with fresh medium without nanoparticles for an additional 0, 2, and 4 hours, where the mitochondrial staining channel is red and cou representing TPT is blue. Scale bars, 10 μm. (**C**) CLSM images for mitochondrial membrane potentials in 4T1 cells after treatment with control, DOX, DTPT, DLTPT, and HA + DLTPT for 4 hours with JC-1–stained mitochondria channel (red, JC-1 aggregate). (**D**) Adenosine triphosphate (ATP) contents of control, d-LND, DOX, DTPT, DLTPT, and HA + DLTPT were detected after incubation with 4T1 cells for 4 hours. (**E**) Immunohistochemical staining images of cytochrome C. Scale bar, 25 μm.

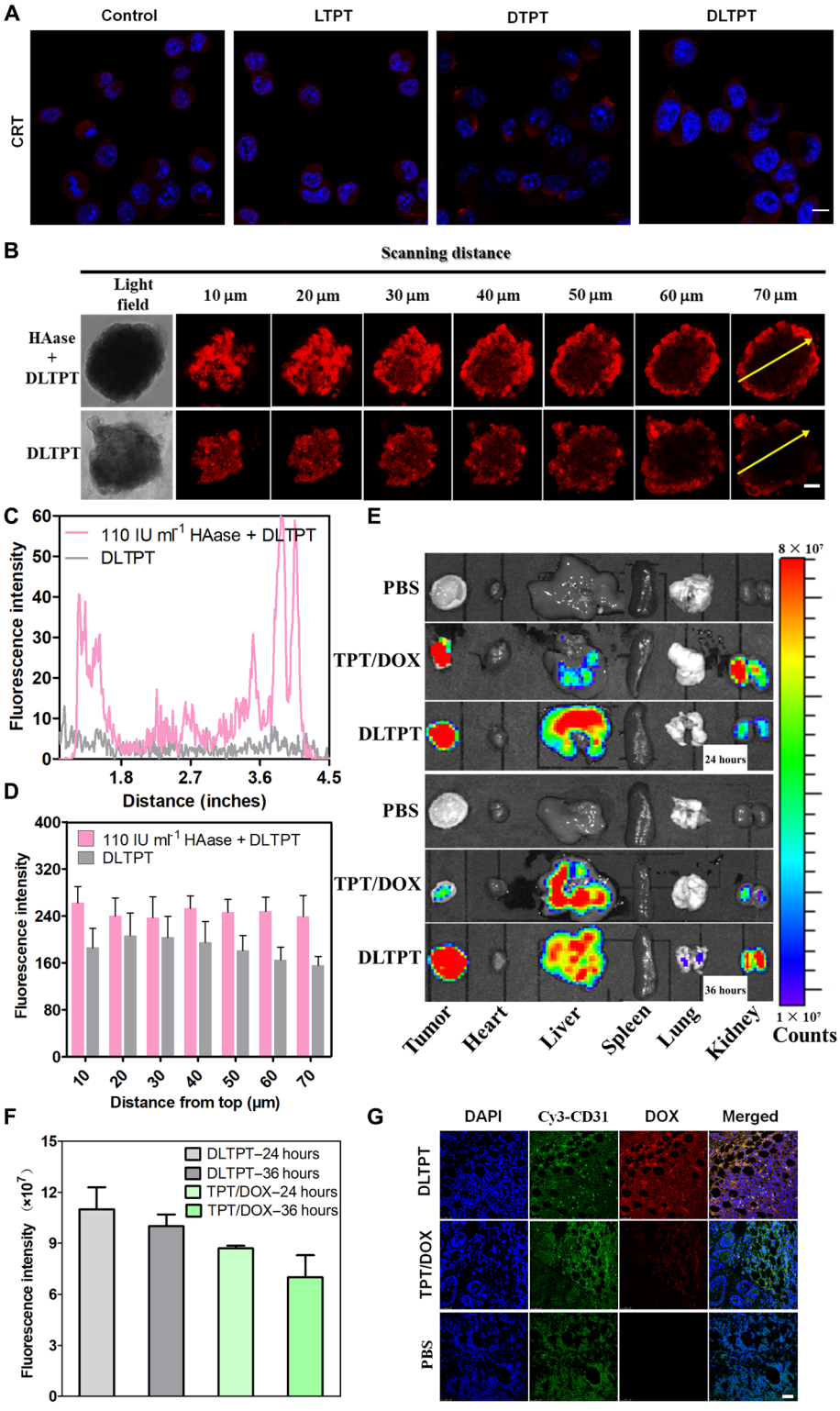

Fig. 4. In vitro permeability and in vivo targeting ability of DLTPT. (**A**) CLSM images of CRT exposure secretion in 4T1 cells after treating with control, LTPT, DTPT, and DLTPT. Red and blue represent CRT signals and nucleus, respectively. Scale bar, 10 μm. (**B**) CLSM images, (**C**) regional coexistence fluorescence profiles (along with yellow arrow at 70 μm), and (**D**) quantitative analysis of DLTPT and HAase + DLTPT (incubation with HAase for 4 hours) incubated with 4T1 multicellular tumor spheroids (MTSs) for 6 hours (means ± SD, $n = 3$; scale bar, 100 μm). (**E**) Ex vivo fluorescence distribution of different tissues and (**F**) quantitative analysis of tumor tissues after administration with phosphate-buffered saline (PBS), TPT/DOX, and DLTPT for 24 and 36 hours in 4T1 tumor model mice. (**G**) Fluorescence intensity of frozen sections of tumor tissues detected by confocal laser, the core dyed by 4′,6-diamidino-2-phenylindole (DAPI; blue), the blood vessels stained with CD-31 mouse antibodies (green), and the nanoparticles represented with the red color (scale bar, 50 μm).

could improve the tumor targeting of DLTPT. The fluorescence intensity of TPP/DOX decreased from 24 to 36 hours after injection, which was indicative of the rapid clearance of positively charged TPT/DOX. However, the fluorescence intensity of DLTPT maintained similar levels from 24 to 36 hours, reflecting the retention capacity of DLTPT. Thereafter, representative tumor tissues from each group were sectioned for immunohistochemical staining. The fluorescence signal in the tumor for the DLTPT group was stronger than that of the control and TPT/DOX groups (Fig. 4G), which was consistent with the in vivo imaging results. Collectively, these findings showed that our designed multifunctional DLTPT could enhance the targeting ability and improve the penetration of DLTPT due to the tumor-homing effect of HA and the HAase-triggered degradation of the HA corona within the tumor.

Antitumor effect in vivo

Furthermore, we evaluated the in vivo therapeutic efficacy using 4T1 tumor–bearing BALB/C mice. The experiment lasted 17 days, and the treatment was conducted on the 7th, 10th, 14th, 17th, and 21st day after tumor inoculation (Fig. 5A). After 17 days of treatment, a much improved antitumor efficacy was observed with DLTPT treatment compared with DOX and DTPT treatments, as evidenced by the decrease in the relative tumor volume (Fig. 5B), reflecting a combinational effect for the combined use of DOX and LND in breast cancer therapy. Notably, after combining DLTPT with anti–PD-L1, the better antitumor efficacy was observed compared with DLTPT (*$P < 0.05$), possibly due to the immune response induced by the addition of anti–PD-L1. Moreover, only slight body weight variations were observed in mice after being treated with phosphate-buffered saline (PBS), DTPT, DLTPT, and DLTPT + anti–PD-L1, while obvious weight loss was observed after DOX treatment (Fig. 5C). The weight loss observed in DOX treatment could be attributed to the unacceptable side effects arising from DOX, which were verified by the hematoxylin and eosin (H&E) staining of the heart section (fig. S8). It was notable that nanoformulations, including DTPT, DLTPT, and DLTPT + anti–PD-L1, could protect the heart from the side effects of DOX, which were distinguished from the irregular and incompact heart sections of the DOX group (fig. S8). Moreover, compared with the other groups, histological and immunohistochemical analyses showed that DLTPT + anti–PD-L1 could induce most cell apoptosis (Fig. 5, D and E). Collectively, the results fully authenticate that the combination strategy of chemotherapy and immune checkpoint blockade could inhibit tumor growth to a maximum extent.

In vivo immune response

To evaluate the immune response, immune cells from the spleen, lymph node, and tumor were analyzed via flow cytometry. The expressions of CD80 and CD86 were used as markers of mature DCs, which could activate T cells (*40*). Compared with the PBS group, the number of $CD11c^+CD80^+$ and $CD11c^+CD86^+$ cells from lymph node in the DLTPT group increased, and an even larger increase was observed in the DLTPT + anti–PD-L1 group (*$P < 0.05$; Fig. 5, F and G, and fig. S9, A and B). A similar phenomenon was observed in spleen (Fig. 5, H and I, and fig. S9, C and D). This suggested that the combination of DOX and LND can induce more DC maturation, and the addition of anti–PD-L1 could further promote DC maturation. In addition, the number of $CD8^+$ T cells significantly increased (*$P < 0.05$) after DLTPT + anti–PD-L1 treatment (Fig. 5, J and K, and fig. S9, E to G), indicating that anti–PD-L1 could enhance the activation of cytotoxic T cells. There was no difference in ratio of $CD4^+$ and $CD8^+$ T cells/T_{reg} between the DLTPT + anti–PD-L1 group and the DLTPT groups (Fig. 5, L and M). Similarly, immunohistochemical results demonstrated that DLTPT + anti–PD-L1 treatment facilitates the increase in the number of $CD4^+$ and $CD8^+$ T cells (Fig. 5N). Furthermore, the decrease in interleukin-10 (IL-10) and the increase in tumor necrosis factor–α (TNF-α) for the DLTPT + anti–PD-L1 group indicated that the treatment could promote the macrophage phagocytic activity and generate a comparable level of TNF-α to stimulate DCs (Fig. 5N and fig. S9H). Moreover, observations using immunohistochemistry for PD-L1 expression levels within the tumor showed increased levels in the PBS, DOX, DTPT, and DLTPT groups, but decreased expression in the DLTPT + anti–PD-L1 group (Fig. 5N). These results from our anti–PD-L1 combination therapy demonstrated that DLTPT stimulated the proinflammatory environment and induced immunological effects in vivo.

Efficacy of metastasis inhibition

As is well known, cancer metastasis accounts for most of therapy failure and cancer-related death. To evaluate the potential of resisting tumor metastasis of DLTPT + anti–PD-L1 by activating the immune system, the lung metastasis model was established by intravenous injection of 4T1 luciferase cells on the third day after primary tumor surgical resection at the end of treatment. The tumor metastasis condition was observed by bioluminescence imaging every 3 days after intraperitoneal injection of D-luciferin potassium solution on the determined intervals (Fig. 6A). At day 3, the mice treated with all groups without bioluminescence were observed. However, when the time prolonged to day 6, lung metastasis was observed in the PBS, DOX, and DTPT groups, and the intensity of bioluminescence increased gradually with time. On the contrary, DLTPT can efficiently inhibit metastasis with faint bioluminescence even at day 9. Moreover, with the combination of anti–PD-L1, DLTPT + anti–PD-L1 has the best potential of antimetastasis without obvious bioluminescence from in vivo lung image (Fig. 6B). This was further confirmed by H&E staining of lung tissues (Fig. 6C). Compared with the positive results of the DLTPT + anti–PD-L1 group, other groups, including PBS, DOX, DTPT, and DLTPT, showed different degrees of cancerization. It is suggested that anti–PD-L1 combined with DLTPT could overcome weak immune response from chemotherapy and low therapeutic response (~20%) from anti–PD-L1 when used alone, showing prominently tumor metastasis inhibition.

Motivated by antigen-specific $CD8^+$ CTL-mediated tumor suppression in the above studies, the immune memory response induced by the DLTPT + anti–PD-L1 treatment was evaluated using resectional rechallenge tumor models (fig. S10A). All of the primary tumors in the mice were removed 4 days after the last intraperitoneal injection of anti–PD-L1. Thirty days later, these mice were challenged with an intravenous injection of 4T1-Luc tumor cells and observed using bioluminescence imaging every 2 days. The survived three mice in each group were chosen to detect the lung metastasis behavior. After 12 days of observations, although metastases occurred in all groups, DLTPT + anti–PD-L1 showed the lowest bioluminescence intensity compared with other groups and the longer survival rate compared with the PBS, DOX, and DTPT groups (fig. S10B), indicating better long immune memory was activated after being treated with DLTPT + anti–PD-L1. H&E staining images also confirmed

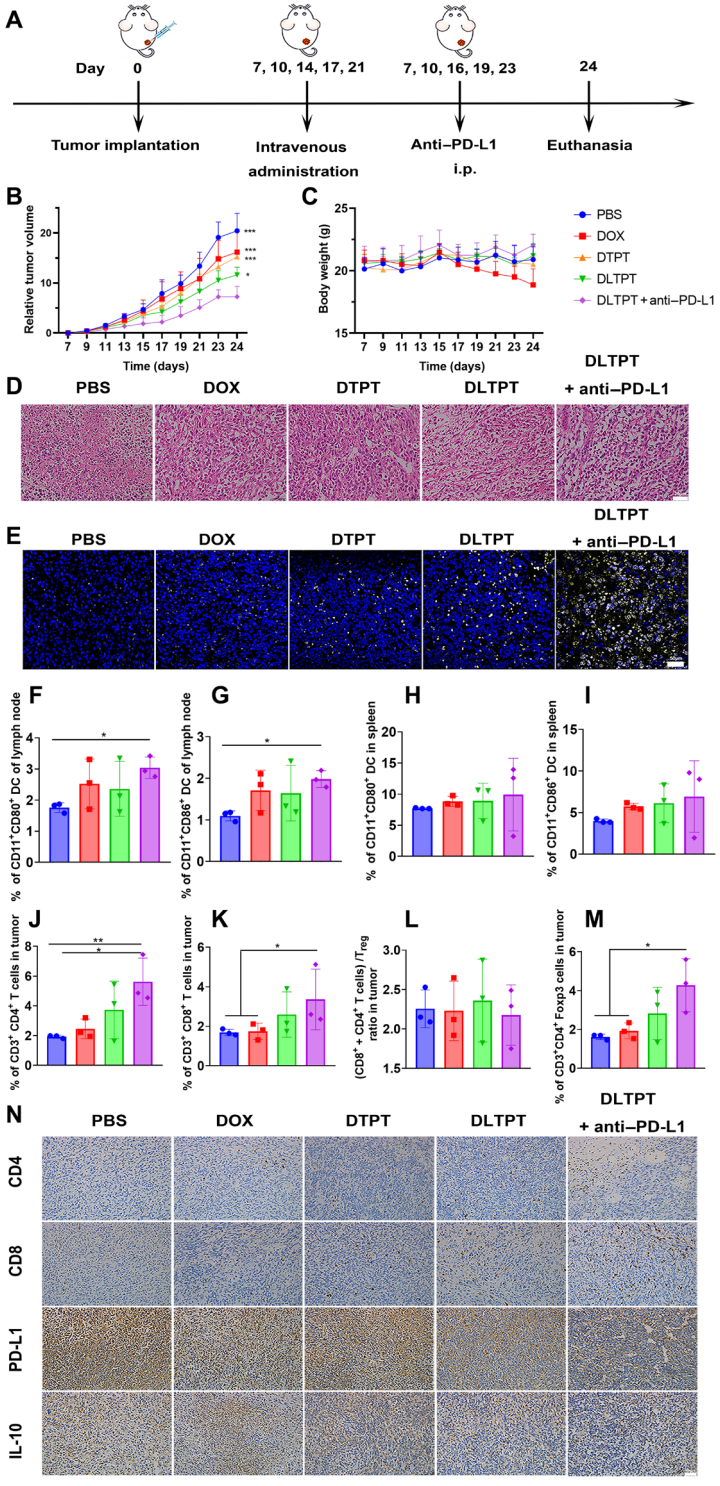

Fig. 5. In vivo antitumor efficiency in 4T1 tumor model and immune response induced by combinatorial therapy. (**A**) Schematic diagram of therapy timeline. i.p., intraperitoneal. (**B**) Relative tumor volume and (**C**) body weight of mice with PBS, DOX, DTPT, DLTPT, and DLTPT + anti–PD-L1 formulations at the end of each treatment (means ± SD, $n = 6$; symbol on each column represents statistical difference compared with DLTPT + anti–PD-L1; $^{*}P < 0.05$, $^{**}P < 0.01$, and $^{***}P < 0.001$). (**D**) Representative hematoxylin and eosin (H&E) for tumors; blue represents nuclei, and red are intercellular substance. Scale bar, 20 μm. (**E**) Terminal deoxynucleotidyl transferase–mediated deoxyuridine triphosphate nick end labeling (TUNEL) staining analysis for 4T1 tumors; normal and apoptosis cells are blue and yellow, respectively. Scale bar, 50 μm. (**F**) $CD11c^+$ $CD80^+$ cells in the lymph node, (**G**) $CD11c^+$ $CD86^+$ cells in the lymph node, (**H**) $CD11c^+$ $CD80^+$ cells in the spleen, (**I**) $CD11c^+$ $CD86^+$ cells in the spleen, (**J**) $CD4^+$ T cells, (**K**) $CD8^+$ T cells, (**L**) the ratio of ($CD8^+$ T and $CD4^+$ T cells) and T_{reg} and (**M**) $CD3^+CD4^+$ Foxp3 (T_{reg}) in tumor (means ± SD, $n = 3$; $^{*}P < 0.05$ and $^{**}P < 0.01$). (**N**) Immunohistochemical staining CD4, CD8, PD-L1, and interleukin-10 (IL-10) from 4T1 tumor sections. Blue represents nuclei, and feature expression cells are brown. Scale bar, 50 μm.

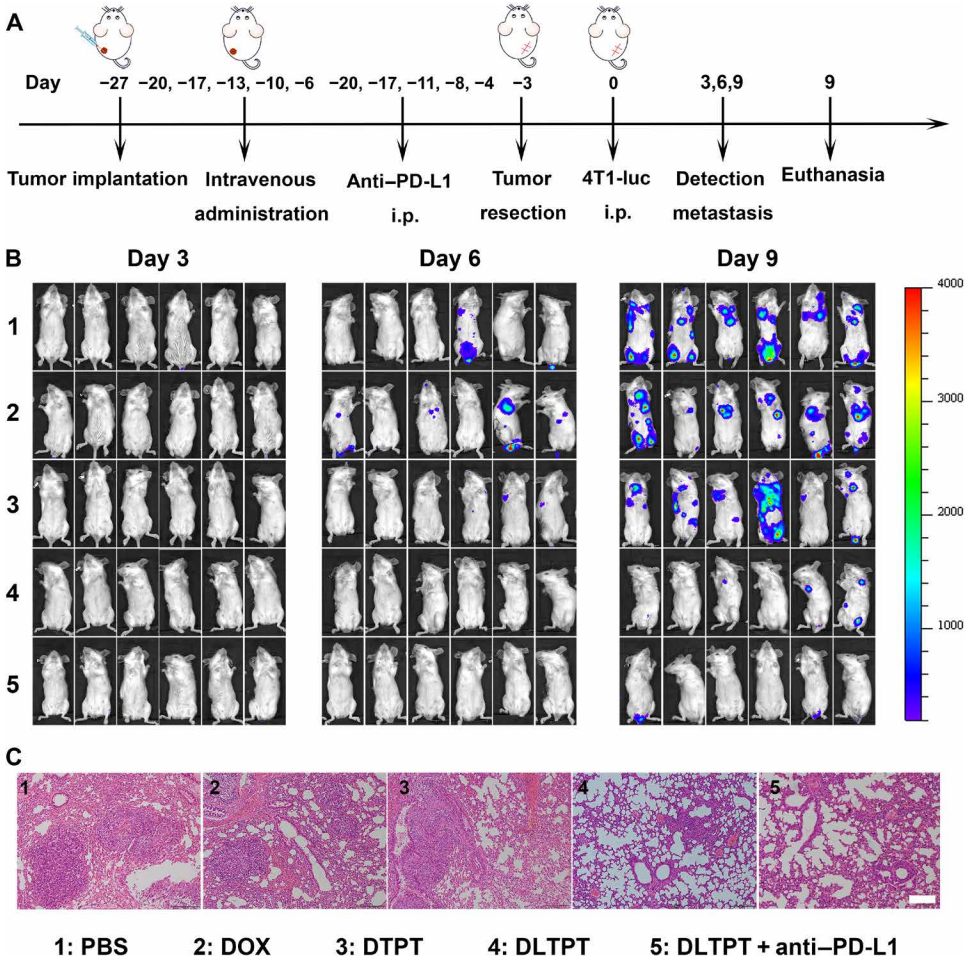

Fig. 6. Antimetastasis effect evaluation. (**A**) Schematic diagram of lung metastasis experiment timeline. (**B**) Inhibition of lung metastasis detected by bioluminescence imaging. (**C**) H&E staining of ex vivo lungs in lung metastasis 4T1 tumor–bearing mice. Scale bar, 100 μm.

the above result (fig. S10C). Collectively, the above results suggested that the combinatorial therapy could boost antitumor immunity to effectively inhibit tumor metastasis and prolong survival time.

DISCUSSION

In this study, we have constructed cascade-targeting, dual drug-loaded, core-shell intelligent nanocarriers (DLTPT) combined with anti–PD-L1 to treat breast cancer and its metastasis. This combinatorial therapeutic platform showed advantages over other chemo- or immune-therapy strategies, supported by the ability to suppress primary tumors and tumor metastasis. Traditionally, tumor-targeted properties of drug delivery nanoplatforms were achieved on the basis of the EPR (enhanced permeability and retention) effect and receptor-mediated endocytosis (*1*, *3*, *11*). However, they encountered imprecise targeted delivery of multiple chemotherapeutics to specific sites or organelles due to lack of cascade targeting, resulting in low antitumor efficiency and unexpected side effects. However, this dilemma could be circumvented by using our designed DLTPT nanoplatforms. Specifically, the HA shell on the nanoparticles could efficiently deliver DLTPT to specifically targeted tumor sites due to its negatively charged and tumor-homing effect features. Thereafter, the extra- and intratumoral overexpression of HAase further facilitated deep penetration, fast cellular uptake, and quick endosome escape, leading to the sequential and controlled release of DOX within the cytoplasm and LND within the mitochondria due to the mitochondria-targeted core (LTPT) exposure. In addition, the construction of dual drug–loaded nanoparticles with cascade-targeting capabilities (DLTPT) was facile and efficient via electro-interaction of HA-DOX and LTPT and also overcame low DLC problems for most nanoparticle systems (*18*, *19*).

Furthermore, in agreement with the previous studies (*15*), the combination of DOX and LND can improve the antitumor efficiency by the destruction of specific subcellular structures via activating apoptotic signals compared with single chemotherapy (DTPT), because of the accurate delivery of both drugs to their respective therapeutic target sites (Fig. 3). Moreover, no unexpected side effects were observed in this therapy, but the antitumor immunity was activated. Many studies confirmed that chemotherapeutic agents, such as DOX, are known to induce ICD (*23*–*25*). In this study, we also observed that signals provided by ICD cause DC maturation and activation of CTL. However, the up-regulation of PD-L1 expression in tumor cells was also observed. On the basis of the reported studies, the increased PD-L1 expression in tumor cells would cause PD-L1–mediated T cell exhaustion after chemotherapy (*31*–*33*), indicating that the current DLTPT-induced CTL activation combined

with chemotherapy would not completely inhibit tumor growth. However, reduced PD-L1 was observed in tumor cells after treatment with anti–PD-L1 inhibitor (an immunosuppression checkpoints inhibitor) and DLTPT, suggesting the efficacy of the activity of the anti–PD-L1 inhibitor for tumor regression. Increased $CD8^+$ T cell counts in tumors and the elevated antigen-specific TNF-α observed in tumor suggested that the combination of anti–PD-L1 inhibitor can block negative signals delivered by PD-L1, resulting in the generation of tumor-specific immunity and effective suppression of primary tumors and tumor metastasis.

Collectively, the proposed combined cascade-targeting, chemoimmune therapy strategy may offer opportunities for improving the drug targeting efficiency, boosting the immune response and combinationally maximizing the therapeutic efficacy. The proposed strategy has the potential to overcome the drawback associated with the lack of active-targeting abilities for clinically used chemotherapeutics resulting in unwanted side effects and the low therapeutic response (~20%) for clinical application of a single dose of anti–PD-L1 (*34*–*35*). Furthermore, most components used in this study, such as DOX and anti–PD-L1, are all U.S. Food and Drug Administration–approved agents, and PLLA is a widely used biodegradable polymer generally exhibiting good biocompatibility, which endows promising clinical translation prospects of this combinational platform for solid tumor treatment. However, the amount of active targeting and the molecular weight of HA and PLLA used to construct the nanoplatform should be thoroughly considered. In addition, the inherent complexity of the combinational platform requires more efforts toward the biocompatibility evaluation process, such as the toxicity, and clearance. Further efforts also need to be concentrated on simplifying the nanosystem design, and maintaining their effective functionalities, to ideally fabricate a "simple but effective" nanosystem for accelerated clinical translation.

In conclusion, we have successfully combined dual-drug chemotherapy and immunotherapy to maximize therapeutic efficacy. This intelligent nanoplatform synchronously delivered DOX and LND to specific action sites by surpassing the biological barriers of chemotherapy, including prolonged blood circulation time, enhanced penetration and retention, increased cellular uptake, and organelle-targeted delivery and release. The synergistic effect of DOX and LND increased the anticancer effect and promoted the production of CTLs. Moreover, the combination of DLTPT with anti–PD-L1 in vivo triggered stronger immune response to inhibit the primary tumor growth and tumor metastasis. We believe that our strategy is highly valuable for developing an advanced cascade-targeting nanosystem to achieve efficient drug delivery and strengthen the immune response.

MATERIALS AND METHODS

Materials

4-Carboxybutyltriphenylphosphonium bromide [$TPP^+COOH{\bullet}Br^-$, weight-average molecular weight (M_w) = 443 Da] and HAase were bought from Sigma-Aldrich (St. Louis, MO, USA). LND and D-luciferin potassium salt were provided by Meilun Biotechnology Co. Ltd. (Dalian, China). DOX hydrochloride (DOX·HCl) was bought from Aladdin Co. Ltd. (Shanghai, China). Sodium hyaluronate (HA; M_w = 40 kDa) was purchased from Bloomage Biotechnology Co. Ltd. (Jinan, China). Anti–CD11c-FITC, anti–CD80–phycoerythrin (PE)–cyanine 7 (Cy7), anti–CD86-PE, anti–Foxp3-PE, anti–CD8a–APC (allophycocyanin), anti–CD4-FITC, and anti–CD3e-APC-Cy7 were all offered by Becton, Dickinson and Company (New Jersey, USA). Cytochrome C mouse antibody, JC-1, and ATP Assay Kit were all purchased from Beyotime Institute of Biotechnology (Jiangsu, China). LysoTracker Red DND-99 and MitoTracker Red CM-H_2XRos were purchased from Invitrogen (UK). Anti–PD-L1 antibody (atezolizumab) was purchased from Selleck Chemicals (Houston, USA). Anti-CD31 was purchased from Abcam (Shanghai, China). 4′,6-Diamidino-2-phenylindole (DAPI) was purchased from Yeasen (Shanghai, China). Anti-CRT was provided by Bioss (Beijing, China).

Mouse mammary breast tumor cell line (4T1) was purchased from the Chinese Academy of Science Cell Bank (Shanghai, China). Female BALB/c mice (20 ± 2 g) were purchased from Ensiweier Biotechnology Co. Ltd. (Chongqing, China) and Dashuo Biotechnology Co. Ltd. (Chengdu, China) and kept under specific conditions with free access to standard food and water. All animal experiments were performed under the protocols approved by the Institutional Animal Administration Committee of the Sichuan University (Chengdu, China).

Synthesis and characterization of TPT polymer, d-LND, and HA-DOX

Mitochondria-targeting PLLA (TPT polymer) was synthesized via ring opening polymerization and coupling reaction. The specific synthetic procedures are exhibited in the Supplementary Materials. Briefly, PLLA was synthesized by ring opening polymerization of LLA using $Sn(Oct)_2$ as a catalyst and 1,6-hexanediol (HI) as the initiator. Thereafter, the TPP was reacted with hydroxyl groups of PLLA to produce the TPT polymer. The structure of the synthesized polymer was characterized by ^{1}H NMR spectrum (AV-400, Bruker, USA) using $CDCl_3$ as the solvent, and 0.5% tetramethylsilane was used as the internal standard.

The synthesis of d-LND and HA-DOX was carried out using the coupling reaction method, in which the detailed synthesis procedures are shown in the Supplementary Materials. High-resolution mass spectrometer (LCMS-IT-TOF, Shimadzu, Japan) and ^{1}H NMR (AV-400, Bruker, America) were used for the structural verification.

Preparation of TPT, LTPT, and DLTPT

The preparation of DLTPT was carried out using the following procedure. In brief, both the TPT polymer (2.5 mg) and d-LND (0.5 mg) were dissolved into tetrahydrofuran (THF), followed by ultrasonification for 30 min, in which the mixture was added into 3.3 ml of deionized water dropwise. After stirring overnight, the LTPT was collected via centrifugation. Subsequently, specific amount of HA-DOX dissolved in deionized water was added into the LTPT micellar solution under vortex for 30 s to produce DLTPT. The preparation method of TPT was similar to that of the DLTPT, except that the d-LND and HA-DOX were not included. Particle size, size distribution, and zeta potential were detected by DLS analysis using a Malvern Zetasizer (Nano ZS Malvern, UK). The morphology of LTPT and DLTPT was observed by TEM (Tecnai G2 F20 S-TWIN, American PEI Company). The drug loading content and loading efficiency of both DOX and d-LND in the DLTPT were measured by an ultraviolet spectroscope (U-3900, Japanese Hitachi) and high-performance liquid chromatography (HPLC; M8301AA, Agilent, USA) at wavelengths of 483 and 266 nm, respectively.

Stimuli response and stability of DLTPT

The size, zeta potential, and morphology of DLTPT in response to HAase were monitored by DLS and TEM measurements. One milliliter of DLTPT was incubated with HAase solution (110 U ml^{-1}) at individual solution with pH 5.0 and pH 6.8, respectively. At predetermined time points, the size and zeta potential of DLTPT were assessed by DLS using a Malvern Zetasizer (Nano ZS Malvern, UK) before centrifugation. The morphology of the DLTPT incubated with HAase at pH 5.0 for 4 hours was detected by TEM (Tecnai G2 F20 S-TWIN, American PEI Company). The stability of the DLTPT under different conditions, including diluted by deionized water and incubated with serum-rich medium and pH 7.4 buffer solution, was studied by DLS analysis.

In vitro drug release behavior

The release behavior of DLTPT was performed via a dialysis procedure. DLTPT (1 ml) was first incorporated into the dialysis bag [MWCO (molecular weight cutoff), 1000 Da] before immersing in large-volume centrifuge tubes containing 25 ml of the respective medium (i.e., pH 7.4 and pH 6.8 + 110 IU ml^{-1} HAase, pH 5.0 + 110 IU ml^{-1} HAase, and pH 5.0 + 110 IU ml^{-1} HAase + 10 mM GSH) under constant shaking at 37°C. At predetermined intervals, 1 ml of the external released medium was taken out and replaced by the same amount of corresponding released medium to ensure volume consistency. The concentration of the released DOX was detected by a fluorescence detector (F-7000, Japanese Hitachi) at excitation of 485 nm. Similarly, the concentration of the d-LND was detected by HPLC by using acetonitrile/water containing 0.1% TFA at 1 ml/min and detected by UV absorbance at 266 nm. The experiment was performed in triplicates, and the data were indicated as means ± SD.

In vitro cellular studies

4T1 and luciferase-transfected 4T1-Luc cancer cells were cultured at 37°C using commercially available RPMI-1640 medium containing 10% fetal bovine serum and 1% penicillin-streptomycin using the standard cell culture procedure.

Cascade-targeting evaluation in vitro

To track the intracellular fate of the DLTPT after being internalized by the cells, the endo-lysosomal escape ability of the DLTPT was characterized. Briefly, 4T1 cells were seeded in glass-bottomed dishes and cultured for 24 hours at 37°C. Afterward, the cells were incubated with DLTPT (DOX, 5 μg ml^{-1}) and HA + DLTPT [cells were pretreated with HA aqueous solution (10 mg ml^{-1}) for 2 hours before the addition of DLTPT; DOX, 5 μg ml^{-1}] for 2 hours. At the end of the incubation, the nanoparticles containing solutions were removed followed by replacing with fresh culture medium without nanoparticles, and the cells were incubated for another 0, 2, and 4 hours, respectively. At predetermined time points, the cells were washed with cold PBS and stained with a commercial Lysotracker Red (100 nM) for 40 min. Last, these cells were washed with cold PBS and observed under a confocal laser scanning microscope (Zeiss, LSM880).

The mitochondrial-targeted delivery of d-LND by the internalized DLTPT was evaluated. Briefly, the d-LND within the TPT core was substituted by cou to facilitate the tracking of the mitochondria-targeting capacity. 4T1 cells were seeded in glass-bottomed dishes for 24 hours at 37°C before treatment with DLTPT for 2 hours. The culture medium was then replaced by a fresh culture medium without nanoparticles and incubated for another 0, 2, and 4 hours. At the predetermined time points, the cells were washed with cold PBS for two times before staining with 200 nM Mito-tracker Red for 30 min for visualization using CLSM.

Mitochondrial membrane potential analysis

Mitochondria membrane potential change was measured using the JC-1 and imaged by CLSM. In brief, 4T1 cells were seeded in the 12-well plates for 24 hours. Then, control, DOX, DTPT, DLTPT, and HA + DLTPT were added to each well (DOX, 5 μg ml^{-1}; HA aqueous solution for 2 hours before the addition of DLTPT), followed by incubation for 4 hours. Control experiments were conducted by adding only culture medium. At the end of the incubation, the cells were washed by PBS for two times before incubation with JC-1 at 37°C for 30 min in the dark. Last, the cells were imaged by CLSM.

Cytochrome C release

The amount of cytochrome C released from the mitochondria into the cytoplasm was analyzed by immunohistochemical staining using cytochrome C mouse antibody. First, 4T1 cells were seeded onto a cover glass and incubated for 24 hours. Afterward, the cells were treated with control, d-LND, DOX, DTPT, DLTPT, and HA + DLTPT (DOX, 5 μg ml^{-1}), respectively. After incubation for 4 hours, the cells were fixed with 4% paraformaldehyde for 20 min and then treated with H_2O_2 (3%, v/v), blocking buffer, primary antibody anti–cytochrome C (Beyotime Institute of Biotechnology, China), enhanced secondary antibody, and enhanced streptavidin horseradish peroxidase conjugate serially. Subsequently, the samples were visualized using a diaminobenzidine (DAB) kit before imaging with an optics microscope to detect the released cytochrome C.

ATP content analysis

4T1 cells were seeded in six-well plates and cultured for 24 hours. Thereafter, the cells were incubated with DOX, d-LND, DTPT, DLTPT, and HA + DLTPT for 4 hours (DOX, 5 μg ml^{-1}). Later, the cells were lysed, in which the cell lysates were collected for the quantification of ATP content using a commercial ATP assay kit (Beyotime Institute of Biotechnology, Jiangsu, China).

Expression of CRT analysis

The expression of CRT exposure on the surface of cells was analyzed by CLSM. 4T1 cells were seeded in glass-bottomed dishes and cultured for 12 hours at 37°C. Thereafter, the cells were incubated with control, LTPT, DTPT, and DLTPT for 6 hours before the staining with anti-CRT primary antibodies (5 μg ml^{-1}) overnight at 4°C after 4% paraformaldehyde fixation of 4T1 cells, and the cells were stained with Cy5-conjugated monoclonal secondary antibodies (6 μg ml^{-1}) for 90 min at 37°C, followed by imaging with a confocal microscopy.

In vitro penetration analysis

MTSs based on 4T1 tumor cells were constructed to detect the penetration behavior of nanoparticles. First, 4T1 tumor cells were seeded in 96-well plates that were coated with a sterile 2% low-melting agarose. The cells were allowed to grow for several days to obtain the MTSs. the MTSs were transferred to confocal dishes followed by treating the MTSs with DLTPT and DLTPT + HAase [pretreated with HAase (110 IU ml^{-1}) for 4 hours in advance] for 6 hours.

Thereafter, the MTSs were fixed with 4% paraformaldehyde for 20 min, followed by washing with PBS before being observed using CLSM.

In vivo distribution

BALB/c mice were subcutaneously inoculated with 1.5×10^5 4T1 cells on their right flank. After 7 days, the mice were randomly divided into three groups and intravenously injected with PBS, DLTPT, and TPT/DOX (DOX, 5 mg kg^{-1}). At predetermined intervals, the mice were euthanized, in which the major organs including heart, liver, spleen, lung, kidney, and tumors of each mouse were isolated for ex vivo imaging. The accumulation of nanoparticles in those major organs and the tumors was evaluated by measuring the fluorescence signal within the harvested tissues using an IVIS Spectrum system (Caliper, MA, USA) at 24 and 36 hours, respectively. In addition, the tumors were further analyzed by embedding the tumors in cryo-solution before freezing and cryosectioned using a freezing slicer (Leica cm2860 UV). The cryosectioned slices were infiltrated with 5% serum tris-buffered saline solution for 1.5 hours. Subsequently, the frozen slices were then incubated with anti-CD31 (2 μg ml^{-1}) at 4°C for 12 hours, followed by incubation with anti-rabbit immunoglobulin G H&L (2 μg ml^{-1}) at 37°C for 2 hours. Last, the frozen slices were tinted with DAPI (0.5 μg ml^{-1}) before mounting with an antifluorescence quenching agent. Last, the samples were observed by CLSM.

In vivo antitumor assessment

The mice comprised 4T1 cell–induced tumor used for antitumor assessment with a tumor volume of ~50 mm^3. The mice were randomly divided into five groups ($n = 6$) and intravenously injected with different formulations twice a week for five times as follows: (i) PBS, (ii) DOX, (iii) DTPT, (iv) DLTPT, and (v) DLTPL + anti–PD-L1 [LND (2.5 mg kg^{-1}), DOX (5 mg kg^{-1}), and anti–PD-L1 (5 mg kg^{-1}) for the first two treatments and anti–PD-L1 (2.5 mg kg^{-1}) for the last three treatments]. Tumor sizes and animal weight were monitored every 2 days, and the tumor volume was calculated using the following formula: $V = (L \times W^2)/2$, where L and W are the larger and smaller diameter of the tumor, respectively. At the end point, the mice were euthanized where their spleens, lymph nodes, and tumors were harvested. The harvested tissues were homogenized to produce single-cell suspension following fluorescence labeling with appropriate antibodies and subsequent flow cytometry analysis. For the analysis of DC, the single-cell suspensions of spleen and lymph nodes were stained with anti–CD11c-FITC, anti–CD80-PE-Cy7, and anti–CD86-PE. For analysis of $CD8^+$ T cells and T_{regs}, the single-cell suspensions of the tumors were stained with anti–Foxp3-PE, anti–CD8a-APC, anti–CD4-FITC, and anti–CD3e-APC-Cy7. Meanwhile, major organs and tumors were fixed with 4% paraformaldehyde for the subsequent H&E, terminal deoxynucleotidyl transferase–mediated deoxyuridine triphosphate nick end labeling (TUNEL), and immunohistochemical staining, including CD8, CD4, TNF-α, IL-10, and PD-L1.

Inhibition of metastases evaluation

The antimetastatic potential of the nanoformulations was assessed via in vivo lung metastasis model. First, 4T1 tumor–bearing BALB/c mice were established as described above. When the tumor volume reached ~50 mm^3, the mice were randomly divided into five groups ($n = 6$) and intravenously treated with the same formulations as mentioned above, including PBS, DOX, DTPT, DLTPT, and DLTPT + anti–PD-L1. The primary tumors of the mice were surgically removed after the last treatment. Then, 3 days after the surgery, these mice were intravenously administrated with 2×10^5 4T1-Luc cells. To detect the metastasis process, bioluminescence imaging was taken every 3 days. Briefly, each mouse was intraperitoneally administered with 0.2 ml of D-Luciferin potassium salt (15 mg/ml) before the image was taken 10 min after the administration. In the end, all the mice were euthanized and the lungs were harvested for H&E.

Statistical analysis

Differences among groups were estimated by the analysis of variance (ANOVA) representing at least three independent experiments. Statistical significance was set at $^*P < 0.05$, $^{**}P < 0.01$, and $^{***}P < 0.001$, as indicated in the figures.

SUPPLEMENTARY MATERIALS

Supplementary material for this article is available at http://advances.sciencemag.org/cgi/content/full/7/6/eaba0776/DC1

View/request a protocol for this paper from *Bio-protocol*.

REFERENCES AND NOTES

1. D. B. Bobo, K. J. Robinson, J. Islam, K. J. Thurecht, S. R. Corrie, Nanoparticle-based medicines: A review of FDA-approved materials and clinical trials to date. *Pharm. Res.* **33**, 2373–2387 (2016).
2. R. Liu, Y. An, W. F. Jia, Y. S. Wang, Y. Wu, Y. H. Zhen, J. Cao, H. L. Gao, Macrophage-mimic shape changeable nanomedicine retained in tumor for multimodal therapy of breast cancer. *J. Control. Release* **321**, 589–601 (2020).
3. H. Cai, X. H. Dai, X. M. Wang, P. Tan, H. Y. Zhu, L. Gu, Q. L. Luo, X. L. Zheng, Z. Q. Li, H. Zhang, Z. W. Gu, Q. Y. Gong, K. Luo, A nanostrategy for efficient imaging-guided antitumor therapy through a stimuli-responsive branched polymeric prodrug. *Adv. Sci.* **6**, 1903243 (2020).
4. W. Yu, R. Liu, Y. Zhou, H. Gao, Size-tunable strategies for a tumor targeted drug delivery system. *ACS Cent Sci.* **6**, 100–116 (2020).
5. D. Huo, X. Jiang, Y. Hu, Recent advances in nanostrategies capable of overcoming biological barriers for tumor management. *Adv. Mater.* **32**, 1904337 (2020).
6. Q. Sun, Z. Zhou, N. Qiu, Y. Shen, Rational design of cancer nanomedicine: Nanoproperty integration and synchronization. *Adv. Mater.* **29**, 1606628 (2017).
7. J. Cao, D. Huang, N. A. Peppas, Advanced engineered nanoparticulate platforms to address key biological barriers for delivering chemotherapeutic agents to target sites. *Adv. Drug Deliv. Rev.* **167**, 170–188 (2020).
8. Z. Luo, Y. Dai, H. Gao, Development and application of hyaluronic acid in tumor targeting drug delivery. *Acta Pharm. Sin. B* **9**, 1099–1112 (2019).
9. R. Liu, W. Xiao, C. Hu, R. Xie, H. Gao, Theranostic size-reducible and no donor conjugated gold nanocluster fabricated hyaluronic acid nanoparticle with optimal size for combinational treatment of breast cancer and lung metastasis. *J. Control. Release* **278**, 127–139 (2018).
10. W. Zhou, H. Yu, L.-J. Zhang, B. Wu, C.-X. Wang, Q. Wang, K. Deng, R.-X. Zhuo, S.-W. Huang, Redox-triggered activation of nanocarriers for mitochondria-targeting cancer chemotherapy. *Nanoscale* **9**, 17044–17053 (2017).
11. Y. Zhu, Y. He, T. Su, C. R. Li, S. Cai, Z. Wu, D. Huang, X. Zhang, J. Cao, B. He, Exogenous vitamin C triggered structural changes of redox-activated dual core-crosslinked biodegradable nanogels for boosting the antitumor efficiency. *J. Mater. Chem. B* **8**, 5109–5116 (2020).
12. G. Pistritto, D. Trisciuoglio, C. Ceci, A. Garufi, G. D'Orazi, Apoptosis as anticancer mechanism: Function and dysfunction of its modulators and targeted therapeutic strategies. *Aging* **8**, 603–619 (2016).
13. F. Yang, S. S. Teves, C. J. Kemp, S. Henikoff, Doxorubicin, DNA torsion, and chromatin dynamics. *Biochim. Biophys. Acta Rev. Cancer* **1**, 84–89 (2014).
14. H. B. Ruttala, N. Chitrapriya, K. Kaliraj, T. Ramasamy, W. H. Shin, J.-H. Jeong, J. R. Kim, S. K. Ku, H.-G. Choi, C. S. Yong, J. O. Kim, Facile construction of bioreducible crosslinked polypeptide micelles for enhanced cancer combination therapy. *Acta Biomater.* **63**, 135–149 (2017).
15. Y. Li, X. Xu, X. Zhang, Y. Li, Z. Zhang, Z. Gu, Tumor-specific multiple stimuli-activated dendrimeric nanoassemblies with metabolic blockade surmount chemotherapy resistance. *ACS Nano* **11**, 416–429 (2017).

16. H. Mizutani, S. Tada-Oikawa, Y. Hiraku, M. Kojima, S. Kawanishi, Mechanism of apoptosis induced by doxorubicin through the generation of hydrogen peroxide. *Life Sci.* **76**, 1439–1453 (2005).
17. R. Misra, S. Acharya, S. K. Sahoo, Cancer nanotechnology: Application of nanotechnology in cancer therapy. *Drug Discov. Today* **15**, 842–850 (2010).
18. S. Lv, Y. Wu, K. Cai, H. He, Y. Li, M. Lan, X. Chen, J. Cheng, L. Yin, High drug loading and sub-quantitative loading efficiency of polymeric micelles driven by donor-receptor coordination interactions. *J. Am. Chem. Soc.* **140**, 1235–1238 (2018).
19. K. Cai, X. He, Z. Song, Q. Yin, Y. Zhang, F. M. Uckun, C. Jiang, J. Cheng, Dimeric drug polymeric nanoparticles with exceptionally high drug loading and quantitative loading efficiency. *J. Am. Chem. Soc.* **137**, 3458–3461 (2015).
20. X. Yang, C. Hu, F. Tong, R. Liu, Y. Zhou, L. Qin, L. Ouyang, H. Gao, Tumor microenvironment-responsive dual drug dimer-loaded PEGylated bilirubin nanoparticles for improved drug delivery and enhanced immune-chemotherapy of breast cancer. *Adv. Funct. Mater.* **29**, 1901896 (2019).
21. G. Saito, J. A. Swanson, K.-D. Lee, Drug delivery strategy utilizing conjugation via reversible disulfide linkages: Role and site of cellular reducing activities. *Adv. Drug Deliv. Rev.* **55**, 199–215 (2003).
22. F. R. Cheng, T. Su, J. Cao, X. L. Luo, L. Li, Y. J. Pu, B. He, Environment-stimulated nanocarriers enabling multi-active sites for high drug encapsulation as an "on demand" drug release system. *J. Mater. Chem. B* **6**, 2258–2273 (2018).
23. D. Alizadeh, M. Trad, N. T. Hanke, C. B. Larmonier, N. Janikashvili, B. Bonnotte, E. Katsanis, N. Larmonier, Doxorubicin eliminates myeloid-derived suppressor cells and enhances the efficacy of adoptive T-cell transfer in breast cancer. *Cancer Res.* **74**, 104–118 (2014).
24. J. Lu, X. Liu, Y. P. Liao, X. Wang, A. Ahmed, W. Jiang, Y. Ji, H. Meng, A. E. Nel, Breast cancer chemo-immunotherapy through liposomal delivery of an immunogenic cell death stimulus plus interference in the IDO-1 pathway. *ACS Nano* **12**, 11041–11061 (2018).
25. L. Zitvogel, L. Apetoh, F. Ghiringhelli, G. Kroemer, Immunological aspects of cancer chemotherapy. *Nat. Rev. Immunol.* **8**, 59–73 (2008).
26. Y. Fan, R. Kuai, Y. Xu, L. J. Ochyl, D. J. Irvine, J. J. Moon, Immunogenic cell death amplified by co-localized adjuvant delivery for cancer immunotherapy. *Nano Lett.* **17**, 7387–7393 (2017).
27. L. Zitvogel, O. Kepp, L. Senovilla, L. Menger, N. Chaput, G. Kroemer, Immunogenic tumor cell death for optimal anticancer therapy: The calreticulin exposure pathway. *Clin. Cancer Res.* **16**, 3100–3104 (2010).
28. W. Zou, Immunosuppressive networks in the tumour environment and their therapeutic relevance. *Nat. Rev. Cancer* **5**, 263–274 (2005).
29. D. M. Pardoll, The blockade of immune checkpoints in cancer immunotherapy. *Nat. Rev. Cancer* **12**, 252–264 (2012).
30. B. G. Nixon, M. O. Li, Satb1: Restraining PD1 and T cell exhaustion. *Immunity* **46**, 3–5 (2017).
31. M. E. Keir, M. J. Butte, G. J. Freeman, A. H. Sharpe, PD-1 and its ligands in tolerance and immunity. *Annu. Rev. Immunol.* **26**, 677–704 (2008).
32. E. J. Wherry, M. Kurachi, Molecular and cellular insights into T cell exhaustion. *Nat. Rev. Immunol.* **15**, 486–499 (2015).
33. K. M. Mahoney, G. J. Freeman, D. F. McDermott, The next immune-checkpoint inhibitors: PD-1/PD-L1 blockade in melanoma. *Clin. Ther.* **37**, 764–782 (2015).
34. R. Kuai, W. Yuan, S. Son, J. Nam, Y. Xu, Y. Fan, A. Schwendeman, J. J. Moon, Elimination of established tumors with nanodisc-based combination chemoimmunotherapy. *Sci. Adv.* **4**, eaao1736 (2018).
35. C. Robert, J. Schachter, G. V. Long, A. Arance, J. J. Grob, L. Mortier, A. Daud, M. S. Carlino, C. McNeil, M. Lotem, J. Larkin, P. Lorigan, B. Neyns, C. U. Blank, O. Hamid, C. Mateus, R. Shapira-Frommer, M. Kosh, H. Zhou, N. Ibrahim, S. Ebbinghaus, A. Ribas; KEYNOTE-006 investigators, Pembrolizumab versus ipilimumab in advanced melanoma. *N. Engl. J. Med.* **372**, 2521–2532 (2015).
36. J. Nam, S. Son, K. S. Park, W. Zou, L. D. Shea, J. J. Moon, Cancer nanomedicine for combination cancer immunotherapy. *Nat. Rev. Mater.* **4**, 398–414 (2019).
37. M. Shafique, T. Tanvetyanon, Immunotherapy alone or chemo-immunotherapy as front-line treatment for advanced non-small cell lung cancer. *Expert Opin. Biol. Ther.* **19**, 225–232 (2019).
38. L. Zhang, H.-J. Yao, Y. Yu, Y. Zhang, R.-J. Li, R.-J. Ju, X.-X. Wang, M.-G. Sun, J.-F. Shi, W.-L. Lu, Mitochondrial targeting liposomes incorporating daunorubicin and quinacrine for treatment of relapsed breast cancer arising from cancer stem cells. *Biomaterials* **33**, 565–582 (2012).
39. L. Qin, J. Cao, K. Shao, F. Tong, Z. L. Yang, T. Lei, Y. Z. Wang, C. Hu, C. S. Umeshappa, H. L. Gao, N. A. Peppas, A tumor-to-lymph procedure navigated versatile gel system for combinatorial therapy against tumor recurrence and metastasis. *Sci. Adv.* **6**, eabb3116 (2020).
40. B. G. Cha, J. H. Jeong, J. Kim, Extra-large pore mesoporous silica nanoparticles enabling co-delivery of high amounts of protein antigen and toll-like receptor 9 agonist for enhanced cancer vaccine efficacy. *ACS Cent Sci.* **4**, 484–492 (2018).

Acknowledgments: We thank G. Meng (National Engineering Research Center for Biomaterials, Sichuan University) for assistance with images. **Funding:** This work was financially supported by the National Natural Science Foundation of China (no. 51973135), the National Key Research and Development Program of China (2018YFC1106100 and 2018YFC1106103), and the 111 Project (no. B18035). The experiments and studies of J.C. and N.A.P. at the University of Texas at Austin were supported by funds from the Institute of Biomaterials, Drug Delivery and Regenerative Medicine. **Author contributions:** J.C. and H.G. designed the project, with the assistance of N.A.P. Y.H., L.L., and H.M. performed the materials synthesis experiments. Y.H. and L.L. performed in vitro cell experiments and all animal in vivo experiments as well as data analysis. X.Y., S.C., F.T., and H.M. assisted in the in vivo experiments. Y.H., L.L., D.H., J.C., and H.G. wrote the manuscript. D.H., N.A.P., K.L., and B.H. guided the manuscript modification. J.C. and H.G. supervised the whole research. **Competing interests:** The authors declare that they have no competing interests. **Data and materials availability:** All data needed to evaluate the conclusions in the paper are present in the paper and/or the Supplementary Materials. Additional data related to this paper may be requested from the authors.

Submitted 3 November 2019
Accepted 21 December 2020
Published 5 February 2021
10.1126/sciadv.aba0776

Citation: Y. He, L. Lei, J. Cao, X. Yang, S. Cai, F. Tong, D. Huang, H. Mei, K. Luo, H. Gao, B. He, N. A. Peppas, A combinational chemo-immune therapy using an enzyme-sensitive nanoplatform for dual-drug delivery to specific sites by cascade targeting. *Sci. Adv.* **7**, eaba0776 (2021).